Nuclear Engineering and Design 241 (2011) 3824–3838

Contents lists available at ScienceDirect

Nuclear Engineering and Design

journal homepage: www.elsevier.com/locate/nucengdes

Modeling pressure suppression pool hydrodynamics in the ABWR containment

Pravin Sawant, Mohsen Khatib-Rahbar*

Energy Research, Inc., PO Box 2034, Rockville, MD 20847-2034, USA

ARTICLE INFO

Article history:
Received 11 January 2011
Received in revised form 25 June 2011
Accepted 1 July 2011

ABSTRACT

This paper focuses on the assessment of pressure suppression pool hydrodynamics in the advanced boiling water reactor (ABWR) containment under design-basis, loss-of-coolant accident (LOCA) conditions. The paper presents a mechanistic model for predicting various suppression pool hydrodynamics parameters. A phenomena identification and ranking table (PIRT) applicable to the ABWR containment pool hydrodynamics analysis is used as a basis for the development of the model. The highly ranked phenomena are represented by analytic equations or empirical correlations. The best estimate and several sensitivity calculations are performed for the ABWR containment using this model. Results of the sensitivity calculations are also presented that demonstrate the influence of key model parameters and assumptions on the pool hydrodynamics parameters. A comparison of model predictions to the results of the licensing analyses shows reasonable agreement. Comparison of the results of the proposed model to experimental data shows that the model predicted top vent clearance time, the pool swell height, and the bubble breakthrough elevation are within 10% of the data. The predicted pool surface velocity and the liquid slug thickness are within 30% of the measurements, which is considered adequate given the large uncertainties in the experimental measurements.

1. Introduction

Following a postulated design-basis LOCA inside the ABWR containment (see Fig. 1), the increase in drywell pressure results in suppression pool vent clearing and the rapid flow of drywell gases (primarily nitrogen) through the suppression pool into the wetwell gas space. The flow of drywell gases through the drywell to wetwell vents creates large, expanding bubbles at the horizontal vent exits. These bubbles expand against the suppression pool hydrostatic and the gas space pressure, as the air/steam mixture flow continues from the pressurized drywell. As a result, the water ligaments (or liquid slugs) on top of the expanding bubbles accelerate upward, which give rise to the pool swell phenomena that typically last 2–3 s. During this phase, the containment wetwell region is subjected to pressure loads on the suppression pool boundary, drag loads on structures initially submerged in the pool (due to the pressurized and expanding bubbles), and pressure loads on the wetwell gas space (due to the rising pool surface that compresses the wetwell gas space). And finally, the rising pool surface can impact and impose drag loads on structures that are located above the pool level inside the wetwell airspace.

Key wetwell airspace internal structures that will be subjected to the pool swell loads (impact and/or drag loads) are the safety relief valve (SRV) discharge piping, catwalk structure, wetwell-to-drywell vacuum breaker, and access tunnel (ABWR DCD, 1997). To predict the pool swell hydrodynamic loads on these wetwell internal structures, it is essential to determine various pool swell parameters such as the maximum pool surface elevation, peak pool surface velocity, peak wetwell gas space pressure, and peak bubble pressure (before the bubble breakthrough) following a design-basis accident (DBA) LOCA. The swollen level (or the maximum pool swell) determines the drag and hydrodynamic impact loads on wetwell structures that are initially above the pool surface. The pool surface velocity determines the severity of the loads, and the gas bubble and wetwell gas space pressures before the bubble breakthrough determine the pressure loading on the wetwell gas space and the suppression pool structural boundaries.

Historically, ABWR vendors have used their proprietary models and computer codes for analysis of pool swell phenomena and associated hydrodynamic loads. The pool swell analysis presented in the ABWR design control document (DCD) (ABWR DCD, 1997) was performed using the General Electric (GE) proprietary computer code PICSM. This code was validated against the Mark III Pressure Suppression Test Facility (PSTF) data. PICSM is a newer version of

Abbreviations: ABWR, advanced boiling water reactor; COL, combined operating license; DBA, design-basis accident; DCD, design control document; FSAR, Final Safety Analysis Report; GE, General Electric; GOTHIC, Generation of Thermal-Hydraulic Information for Containments; LOCA, loss-of-coolant accident; NRC, United States Nuclear Regulatory Commission; PIRT, phenomena identification and ranking table; PSTF, Pressure Suppression Test Facility; RPV, reactor pressure vessel; STP, South Texas Project; SRV, safety relief valve.

* Corresponding author. Tel.: +1 301 881 0866; fax: +1 301 881 0867.
E-mail address: mkr1@eri-world.com (M. Khatib-Rahbar).

0029-5493/$ – see front matter © 2011 Elsevier B.V. All rights reserved.
doi:10.1016/j.nucengdes.2011.07.002

Nomenclature

A_b	cross-sectional area of the bubble (m^2)
A_{Hf}	total horizontal vent area available for the liquid flow (m^2)
A_{Hg1}	area of the top horizontal vent available for the gas flow (m^2)
A_{Hg2}	area of the middle horizontal vent available for the gas flow (m^2)
A_{SP}	suppression pool surface area (m^2)
A_V	area of the vertical vent pipe (m^2)
C_D	drag coefficient
D	diameter of flow channel (m)
$Dpool_i$	suppression pool annulus inner diameter (m)
$Dpool_o$	suppression pool annulus outer diameter (m)
D_l	length of the longer side of a rectangle (m)
D_s	length of the shorter side of a rectangle (m)
D_{SP}	hydraulic diameter of the suppression pool (m)
d_{Hg1}	hydraulic diameter of the top horizontal vent (for gas flow) (m)
d_{Hg2}	hydraulic diameter of the middle horizontal vent (for gas flow) (m)
d_{Vg}	hydraulic diameter of the vertical vent pipe (for the gas flow) (m)
f	wall friction factor
g	gravitational acceleration (m/s^2)
H_{S0}	total suppression pool depth above the bottom of the bottom horizontal vent (m)
H_{PS}	suppression pool swell height (m)
H_s	top vent centerline submergence at the time of top vent clearance (m)
H_{SL}	thickness of the liquid slug on top of the bubble (m)
k_A	effective gas phase vent form loss coefficient for the top horizontal vent
k_d	drywell connecting vent entrance loss coefficient
k_e	horizontal vent exit loss coefficient
k_{fE}	effective liquid phase vent loss coefficient
k_{gE}	effective gas phase vent loss coefficient
k_{SP}	suppression pool loss coefficient
k_t	90° elbow turning loss coefficient
k_{t1}	standard tee loss (flow through branch)
k_{t2}	standard tee loss (flow through run)
L_H	length of horizontal vent (m)
L_V	total length of vertical and horizontal vents (m)
m_{gb}	bubble mass (kg)
N	number of vertical vents (10 for the ABWR containment)
P	pressure (Pa)
P_B	internal bubble pressure (Pa)
P_B^0	initial pressure inside the bubble (Pa)
P_D	drywell pressure (Pa)
P_∞	pressure outside the bubble (Pa)
P_{WW}	wetwell gas space pressure (Pa)
P_{WW}^0	initial wetwell gas space pressure (Pa)
R	time-dependent radius of the spherical bubble (m)
R_{CAP}	radius of the cap bubble (m)
Re	Reynolds number
Re_b	bubble Reynolds number
t	time (s)
T_D	drywell temperature (°C)
T_{SP}	suppression pool temperature (°C)
u_b	bubble rise velocity (m/s)
u_{gs}	sonic velocity of gas phase (m/s)
$\bar{u}_{gv}$	area averaged gas phase velocity in vertical vent (m/s)
$\bar{u}_H$	area averaged velocity of water inside horizontal vent (m/s)
$\bar{u}_{SP}$	area averaged suppression pool surface velocity (m/s)
u_{tb}	bubble terminal velocity (m/s)
u_{tbCAP}	spherical cap bubble terminal velocity (m/s)
u_{tbSLUG}	slug bubble terminal velocity (m/s)
$\bar{u}$	area averaged velocity (m/s)
$\bar{u}_V$	area averaged velocity of water inside vertical vent (m/s)
V_b	volume of spherical bubble (m^3)
$\dot{V}_b$	volumetric growth rate of spherical bubble (m^3/s)
V_{WW}^0	initial wetwell gas space volume (m^3)
V_{WW}	wetwell gas space volume (m^3)
W_{gCR}	gas phase critical mass flow rate (kg/s)
W_{gb}	rate of change of the bubble mass (kg/s)
W_{gv}	mass flow rate of the drywell gas through the vertical vent pipe (kg/s)
x	water level inside the vertical vent pipe (m)
Z_{bubble}	elevation of the bubble above the top vent centerline (m)
Z_{pool}	elevation of pool surface above the bottom of the suppression pool (m)

Greek symbols

β_1	ratio of diameters for the top horizontal vent (d_{Hg1}/d_{Vg})
β_2	ratio of diameters for the middle horizontal vent (d_{Hg2}/d_{Vg})
ρ	density of fluid (kg/m^3)
ρ_f	density of water inside the suppression pool (kg/m^3)
$\bar{\rho}_g$	average gas phase density (kg/m^3)
ρ_{gB}	gas phase density calculated at the internal pressure of the bubble (kg/m^3)
ρ_{gB}^0	gas density inside the initial bubble (kg/m^3)
ρ_{gD}	drywell gas phase density (kg/m^3)
τ_w	wall shear stress (kg/ms^2)
γ	polytropic constant

the GE proprietary code PSAM which was developed for the Mark II containment design (NUREG-1503, 1994). Kukita et al. (1984) reported that PSAM models the pool swell as a one-dimensional phenomenon. In this model, the air bubbles are assumed to occupy entire area of the pressure suppression pool forming a sheet of uniform thickness. The pool of water above the air bubble is represented by a one-dimensional water slug with a constant thickness equal to the initial submergence height of the vent. Therefore, the PSAM model does not account for the rise of bubbles through pressure suppression pool water as observed in the PSTF experiments. Additional details about this model are not available in the open literature.

The pool swell analysis presented in the Final Safety Analysis Report (FSAR) (South Texas Project [STP] Units 3 and 4 FSAR, 2007) submitted to the United States Nuclear Regulatory Commission (NRC) in support of the combined license (COL) application utilized a methodology that is based on the Generation of Thermal-Hydraulic Information for Containments (GOTHIC) computer code. The GOTHIC-based methodology has also been benchmarked against the Mark III PSTF data (STP Units 3 and 4 FSAR, 2007). Unfortunately, due to its proprietary nature, the addi-

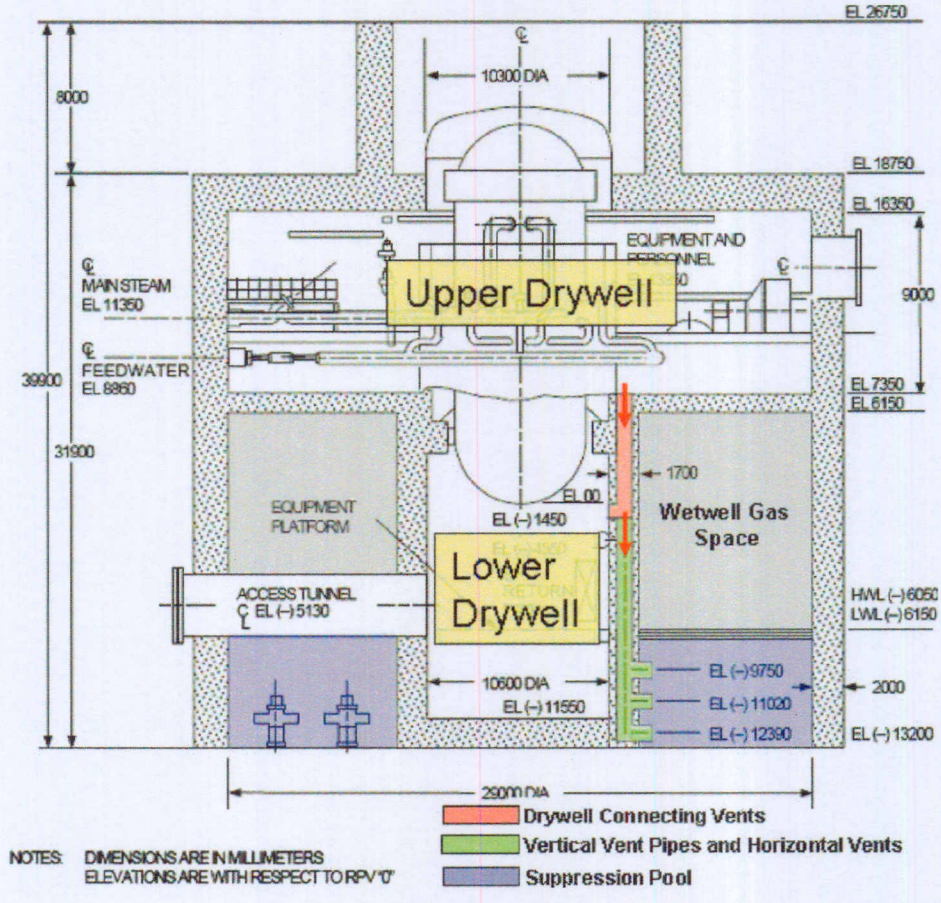

Fig. 1. Schematic of the ABWR containment (ABWR DCD, 1997).

tional details about this methodology are also not available in the open literature.

Yan and Bolger (2010) developed a three-dimensional CFD model to simulate the pool swell process in the PSTF test facility. They reported satisfactory prediction of the vent clearance time and pool surface velocity. Sufficient details about the CFD problem formulation and setup have not been provided by Yan and Bolger (2010), thus making it is difficult to reproduce the CFD results.

In the past, several experimental and theoretical investigations have been performed to study the pool swell and associated hydrodynamic loads in the Mark I and Mark II containments. Chen and Dhir (1982) studied the hydrodynamics of a bubble formed at the exit of a vertical pipe submerged in a pool of water. They performed these experiments by injecting air through the pipe and measured the bubble growth rate and the pressure histories inside the pipe. They also studied the effect of presence of an orifice inside the pipe on the growth of bubbles. Fernandez (1976), Lai and McCauley (1978), Huber et al. (1979), Kiang and Jeuck (1980, 1981), and Kiang and Grossi (1981) performed pool swell experiments in scaled down test facilities simulating the Mark I containment. Similar scaled down experiments applicable to the Mark II containment pressure suppression pool were performed by Kiang and Jeuck (1980) and Kukita et al. (1984). More recently, Gupta et al. (2011) obtained measurements of local dynamic pressure (at the pool bottom, the pool walls, and the gas space) and high speed flow visualization which can be used for the development and validation of the CFD codes. The analytic models have been also developed for the modeling of pool swell in the Mark I and Mark II containment (Glenn and McMaster, 1978; Chan and Vander Vorst, 1978; Huber et al., 1979; Chambre and Nitao, 1981; Widener, 1986). However, these Mark I and Mark II related studies have limited applicability for the ABWR pool swell analysis. Particularly the design of vent system and the pressure suppression pool in the ABWR containment is quite different when compared to the Mark I and Mark II containments.

The objective of this paper is to present analytic models based on fundamental physical principles that are used for the confirmatory prediction of suppression pool hydrodynamics and associated figures-of-merit (i.e., vent clearance, pool surface elevation, pool surface velocity, wetwell gas space and the bubble pressure) under DBA LOCA conditions. A comparison of model predictions against the GOTHIC pool swell analysis results (STP Units 3 and 4 FSAR, 2007) is intended to show the fidelity of the proposed model compared to other available studies. This paper also examines the sensitivity of key figures-of-merit to major model assumptions and governing model parameters. Finally, the paper presents the results of comparison of the proposed model to the BWR Mark III PSTF experimental data.

2. Dominant phenomena

The highly ranked phenomena identified in the PIRT in Table 1 are applicable to the ABWR containment suppression pool swell dynamic response. This PIRT identifies the dominant phenomena

Table 1
PIRT for ABWR containment suppression pool swell dynamic response.

Phenomenon/process	Importance ranking
Mass and energy release from RPV and piping side	
Stored energy in vessel and core assemblies and heat transfer to coolant	L
Decay heat to coolant (short- and long-term)	L
Scram and core power during blowdown	L
RPV two-phase level swell (core and downcomer) and two-phase and single-phase blowdown intervals	L
Two-phase and single phase critical flow	H
Break flow flashing (generation of droplets and vapors)	H
Initial pipe inventory and double ended blowdown interval	H
Drywell atmosphere mass and energy transfer	
Mixing and transport of non-condensable gases and water vapor	H
Droplet transport (break-up, coalescence, evaporation, and droplet suspension or fallout)	H
Heat transfer to drywell heat structures (steam condensation on surfaces) and wall heat transfer	M
Flow in drywell connecting vents	
Two-phase flow regime through drywell connecting vents	M
Flow losses in drywell connecting vents	M
Lower drywell non-condensable gas transport	
Mixing and transport of non-condensable gases from lower drywell to wetwell gas space	L
Flow in horizontal vents	
Vent clearance and fluid inertia	M
Flow through vent (perfect gas, steam, gas-droplet mixture, and choked flow)	M
Flow losses (bends, turns, geometric losses)	H
Effect of back pressure and clearing time, sequential	H
Mass, energy and momentum transfer in suppression pool	
Direct contact condensation of vapors in suppression pool in presence of non-condensable gases	M
Suppression pool mixing and thermal stratification (pool heating)	L
Gas bubble discharge	H
Pool swell and height	M
Bubble penetration	M
Mass, energy, and momentum transfer in wet-well gas space	
Gas sparging through the suppression pool	H
Wetwell pressurization	H
Pool surface rise and compression of gas	H
Wetwell gas/vapor mixing and stratification	L
Heat transfer to wetwell heat structures	L
Long term pool heating of gas	L
Suppression pool bypass leakage	
Flow of vapor mixture directly from drywell to wetwell gas space	L

that are modeled to analyze suppression pool hydrodynamics in the ABWR containment, as described in Section 3 of this paper. The importance rankings assigned in the PIRT were delineated based on the expected impact of the phenomenon on pool swell parameters (i.e., maximum pool surface elevation, peak pool surface velocity, peak wetwell gas space pressure, and peak bubble pressure). The highly ranked phenomena can be broadly classified into four categories based on what the phenomena affect:

(a) drywell pressurization rate;
(b) vent clearance time and flow rate;
(c) formation and growth rate of the bubble; and
(d) the rise and breakthrough of the bubble.

The drywell pressurization rate is a function of the rate of mass and energy release into the drywell from the reactor pressure vessel (RPV) and the piping sides of the break. The break flow from the piping side of the break primarily consists of stored inventory of coolant inside the piping. The break flow from the RPV side is determined by the RPV thermodynamic conditions. Several phenomena are identified in the PIRT that affect the RPV thermodynamic conditions and hence, the break flow rate. However, for the present model, the transient drywell pressure and temperature are specified as boundary conditions. Consequently, the phenomena affecting the drywell pressurization rate are not formulated as part of this paper.

The vent clearance time is the time required for the transfer of water from the drywell-to-wetwell vent system to the suppression pool after a LOCA. Predicting the vent clearance time is essential for modeling the pool swell phenomena because it determines the time required for the initiation of a pool swell following a LOCA. Furthermore, the flow of the drywell gas mixture through the vents following the vent clearance determines the growth rate of the bubble and the magnitude of the pool swell parameters. The parameters/phenomena affecting the vent clearance time include the inertia of water inside the vent system and the suppression pool, the hydrostatic head of water inside the suppression pool, the friction and form losses in the vent system (including the effect of flow regimes), and the back pressure at the exit of the horizontal vents (due to the expanding bubble and the inertia of the liquid slug following the clearance of the top vents).

The flow rate of the drywell gas mixture through the vents following the vent clearance is mainly affected by various pressure losses through the vent system, including the losses due to fluid inertia, spatial acceleration, gravity, friction, and form losses (due to wall friction, flow area contraction/expansion, and bends/turns). Higher pressure losses through the vent system result in a lower vent flow rate and a relatively less severe pool swell response. Therefore, for the pool swell analysis, the assumption of a minimum pressure loss is bounding. Furthermore, the flow of drywell gases through the vent system could reach sonic conditions, thus limiting the discharge of the drywell gas mixture through the vents to the critical mass flow rate.

Predicting the growth rate of the bubble is important because it determines the magnitude of various pool swell parameters. This growth rate is governed by the difference in the pressures inside and outside the bubble. In the present model, the growth rate of the bubble is calculated using the Raleigh equation (Carey, 2007). The phenomena/parameters affecting the inside pressure of the bubble include the vent mass flow rate and the interfacial heat and

mass transfer at the bubble and suppression pool water interface. The interfacial heat and mass transfer at the interface of the bubble is due to the steam (which is part of the drywell gas mixture) at this interface and the cooling of the non-condensable gases in the bubble resulting from the transfer of heat to the suppression pool water. If either the drywell gas mixture or the vent gas flow discharge includes some percentage of steam, the growth rate of the bubble will be lower. The higher growth rate is obtained by assuming that 100% of the atmosphere in the drywell is only occupied by nitrogen. Furthermore, the interfacial heat transfer between the gas bubble and the suppression pool affects both the gas temperature and the growth rate of the bubble. During a LOCA, the drywell air temperature is usually higher than the suppression pool temperature. The reduction in the temperature of the gas in the bubble due to the interfacial heat transfer to the suppression pool water will effectively reduce the growth rate of the bubble. An assumption of 100% nitrogen in the drywell and the absence of the interfacial heat and mass transfer would result in a higher growth rate of the bubble and more bounding predictions for various pool swell parameters.

The outside pressure of the bubble is affected by the hydrostatic head and inertia of the liquid slug on top of the bubble. Additionally, the compression of the wetwell gas space due to a rising suppression pool surface also influences this outside pressure. Pressurization of the wetwell gas space reduces the growth rate of the bubble. Isothermal compression would result in a lower wetwell gas space pressure and a higher bubble growth rate (hence, a higher pool swell height and pool surface velocity). On the other hand, adiabatic compression would result in a higher wetwell gas space pressure and a lower bubble growth rate.

The bubble rise velocity and bubble breakthrough time determine the termination of the pool swell transient. The bubble rises through the suppression pool due to the combined effects of buoyancy and drag forces acting on the bubble. These forces are functions of the size and shape of the bubble. Therefore, the bubble rise velocity depends on the size and shape of the bubble—as the size increases, the buoyancy force on the bubble increases. However, the shape of the bubble also changes with its size. The bubbles formed in the suppression pool during the pool swell transient are relatively large in size (due to the large horizontal vent diameter of 70 cm). They do not exactly match any of the well-known bubble types for which bubble rise velocity measurements are available (see Figs. 11 and 12 of Lahey and Moody, 1993). Judgment is needed to predict the rise velocity of growing bubbles that are being charged from the horizontal vents. Furthermore, the rise velocity of a slug bubble is affected by the presence (or absence) of wetwell gas space pressurization.

3. Mathematical models

Based on the discussion of the dominant phenomena, this section presents the various mathematical models that are used to simulate suppression pool hydrodynamics in the ABWR containment. Note that with the exception of specific geometrical aspects, the proposed models are generally applicable to predictions of hydrodynamic loads in BWRs with different containment configurations (e.g., Mark I and Mark II, etc.).

3.1. Vent clearance

Fig. 2 shows a modeling approach used to simulate the vent clearance phenomenon. In this figure, x indicates the water level inside the vertical vent pipe. A_{Hf}, A_v, and A_{SP} are the total horizontal vent area available for the liquid flow, the cross-sectional area of the vertical vent pipe, and the suppression pool surface area, respectively. k_{fE} indicates the total effective vent form loss coefficient for liquid flow (see Appendix A). Fig. 2 shows that the three horizontal vents (top, middle, and bottom vents) in the ABWR design (shown on the left side) are represented by a single horizontal vent by the present model (shown on the right side). This assumption eliminates the need of separate momentum equation for each horizontal vent leading to the simplification of the model.

The one-dimensional momentum equation is obtained by averaging the area of the three-dimensional momentum equation, namely:

$$\frac{\partial \rho \bar{u}}{\partial t} + \frac{\partial \rho \bar{u}^2}{\partial z} = -\frac{\partial P}{\partial z} - \frac{4\tau_w}{D} + \rho g \tag{1}$$

Furthermore, it is assumed that:

(a) The velocity of water inside the horizontal vent ($\bar{u}_H$) and the suppression pool surface velocity ($\bar{u}_{SP}$) are related to the velocity of water inside the vertical vent pipe $\bar{u}_V$ through the mass continuity equation:

$$\bar{u}_H = \frac{A_V}{A_{Hf}} \bar{u}_V \tag{2}$$

$$\bar{u}_{SP} = \frac{A_V}{A_{SP}} \bar{u}_V \tag{3}$$

(b) The suppression pool surface area (A_{SP}) is very large compared to the areas of the vertical vent pipe and the horizontal vent. Therefore, the pool surface velocity is negligibly small ($\bar{u}_{SP} \approx 0.0$).

(c) The rise in pool surface due to the transfer of vent system water into the suppression pool is accounted for by increasing the suppression pool height (H_{S0}).

(d) The wetwell gas space pressure (P_{WW}) is assumed to be constant at the initial condition.

(e) Pressure drops due to inertia, special acceleration, gravity, and form and friction losses in the vent system are considered. Pressure drops due to inertia, special acceleration, and friction in the suppression pool are neglected due to the negligibly small suppression pool surface velocity.

(f) Pressure at the water surface inside the vertical vent is assumed to be equal to the drywell pressure (i.e., before the vent clearance, the gas flow from the drywell to the vertical vent pipe is very small).

Therefore, integrating Eq. (1) from the surface water inside the vertical vent pipe (point M in Fig. 2) to the suppression pool surface (point N in Fig. 2) results in the following ordinary differential equation representing the water velocity inside the vent:

$$\left(\rho_f x + \rho_f L_H \frac{A_v}{A_{Hf}}\right) \frac{d\bar{u}_V}{dt} - \rho_f \bar{u}_V^2 = (P_D - P_{WW}) - \rho_f k_{fE} \frac{\bar{u}_V^2}{2} + \rho_f g(x - H_{S0}) \tag{4}$$

Subsequently, the water level inside the vertical vent pipe is related to the water velocity by:

$$-\frac{dx}{dt} = \bar{u}_V \tag{5}$$

Eqs. (4) and (5) are solved numerically with the time-dependent drywell pressure used as a boundary condition to calculate the water level inside the vertical vent pipe. Furthermore, the total area of the horizontal vents available for the liquid flow (A_{Hf}) and the effective liquid phase loss coefficient (k_{fE}) are estimated from the water level inside the vertical vent. Appendix A presents the approach for calculating effective vent form loss coefficients for the liquid and gas flow phases.

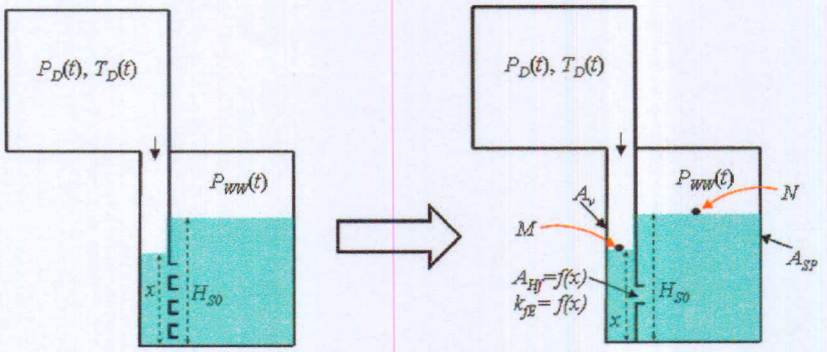

Fig. 2. Modeling approach for simulating the vent clearance phenomenon.

Immediately after the clearance of the top horizontal vent, the drywell air begins to flow into the suppression pool and creates an expanding air bubble at various vent exits. This expanding bubble accelerates the pool surface and exerts a higher pressure on the middle and the bottom vent exits, thus delaying their clearance (i.e., the backpressure effect). Therefore, the assumptions of the negligible pool surface velocity, the constant wetwell gas space pressure, and negligible pressure losses in the suppression pool (e.g., pool inertia) are challenged as the water level drops below the top horizontal vent. Consequently, these assumptions are expected to result in a faster prediction of the clearance of the middle and bottom horizontal vents and in a more bounding estimate of the pool swell parameters.

3.2. Pool swell

The simulation of suppression pool swell behavior consists of solving equations representing the vent system pressure drop (for the gas flow) and the growth rate, rise velocity and location, outside pressure of the bubble; the pool surface velocity and elevation, the wetwell gas space pressure, and thickness of the liquid slug on top of the bubble. The pool swell calculations are initiated as soon as the water level inside the vertical vent pipe drops below the top elevation of the top horizontal vent. The models described below take the input from the vent clearance model (Section 3.1) (effective vent form loss coefficient and total horizontal vent area available for the gas flow/flow of gas), while the drywell pressure and temperature are supplied as boundary conditions.

3.2.1. Vent pressure drop

The vent pressure drop equation is derived from the calculation of gas flow through the vent system following the clearance of the top horizontal vent. Similar to the vent clearance model, all horizontal vents (top, middle, and bottom) are assumed to be represented by a single horizontal vent. However, unlike the vent clearance model above, the elevation of the horizontal vent is fixed at the top horizontal vent elevation (see Fig. 3). This assumption minimizes the thickness of the accelerating liquid slug thereby resulting in more bounding estimates of the pool swell height and surface velocity.

The integration of the one-dimensional area averaged momentum equation [Eq. (1)] from the entrance of the drywell connecting vents to the exit of the horizontal vents by assuming:

(a) All horizontal vents are located at the elevation of the top horizontal vents.
(b) The total area of horizontal vents available for the gas flow (A_{Hg}) and the effective gas phase form loss coefficient (k_{gE}) for vents are obtained from the solution of the vent clearance model presented in Section 3.1. A sensitivity analysis is considered in Section 4 to study the effect of gas phase vent form loss coefficient (k_{gE}).
(c) Only inertial and frictional pressure losses are accounted for (inertial pressure drop and wall friction losses in the horizontal vents are neglected). The pressure drops due to spatial acceleration and gravity are neglected. Since this assumption results in a lower pressure drop and hence, a higher gas phase mass flow rate through the vent system, it is considered bounding for the calculation of pool swell parameters.
(d) The average gas phase density ($\bar{\rho}_g$) is obtained by averaging the drywell and bubble gas densities. The drywell gas density is obtained from the drywell pressure and temperature boundary conditions. The bubble gas density can be calculated by assuming that either isothermal or adiabatic compression of an ideal gas.

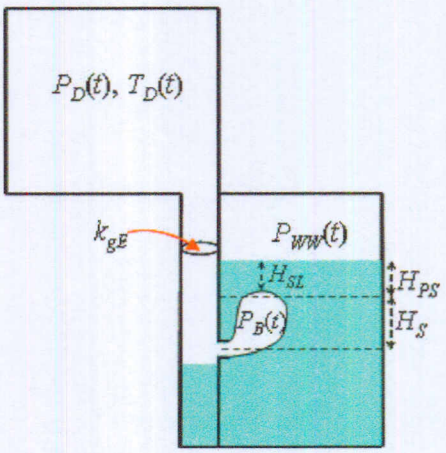

Fig. 3. Estimate of pressure drop through vents.

Therefore, the following equation represents the pressure drop through the vents:

$$\bar{\rho}_g L_V \frac{d\bar{u}_{gV}}{dt} + \left(\frac{fL_V}{d_{Vg}} + k_{gE}\right)\frac{\bar{u}_{gV}^2}{2}\bar{\rho}_g = P_D - P_B \tag{6a}$$

This is further simplified by neglecting the inertial pressure drop (due to a relatively small gas phase density) that leads to the following equation:

$$\left(\frac{fL_V}{d_{Vg}} + k_{gE}\right)\frac{\bar{u}_{gV}^2}{2}\bar{\rho}_g = P_D - P_B \tag{6b}$$

3.2.2. Growth rate of the bubble

The submerged gas bubble that is formed at the exit of the horizontal vents (following the vent clearance) is assumed to be spherical with a time-dependent radius R, internal pressure P_B, expanding against an outside pressure of P_∞, surrounded by suppression pool water with a density of ρ_f.

Assuming that:

(a) The pressure inside the bubble is uniform and equal to the pressure at the exit of the horizontal vent (P_B).
(b) Heat and mass transfers at the bubble interface are neglected.
(c) The pressure outside the bubble is uniform around the bubble and accounts for the liquid slug (which exists on top of the bubble) inertia and the hydrostatic head [see Eq. (31)].
(d) The surface tension effects are negligible.

Therefore, the growth of an idealized spherical bubble is governed by the Rayleigh equation (Carey, 2007) of the form:

$$R\frac{d^2R}{dt^2} + \frac{3}{2}\left(\frac{dR}{dt}\right)^2 = \frac{1}{\rho_f}\left(P_B - P_\infty - \frac{2\sigma}{R}\right) \tag{7a}$$

Even at the initial formation of the bubble, when the radius is minimum (i.e., equivalent to the radius of the horizontal vents), the surface tension contribution is negligibly small ($2\sigma/R < 0.4$) when compared to the pressure difference ($P_B - P_\infty$). The contribution from surface tension continuously decreases as the bubble grows inside the pool. Therefore, the surface tension term can be neglected to arrive at:

$$R\frac{d^2R}{dt^2} + \frac{3}{2}\left(\frac{dR}{dt}\right)^2 = \frac{1}{\rho_f}(P_B - P_\infty) \tag{7b}$$

Furthermore, the volumetric growth rate ($\dot{V}_b$) and the rate of change of the submerged bubble mass (W_{gb}) are governed by:

$$\frac{dV_b}{dt} = \dot{V}_b = 4\pi R^2\frac{dR}{dt} \tag{8}$$

and

$$W_{gb} = \frac{dm_{gb}}{dt} = \rho_{gb}\frac{dV_b}{dt} \tag{9}$$

The conservation of mass requires that the rate of change in the mass of the bubble (W_{gb}) is the same as the mass flow rate of the drywell gas through the vertical vent pipes (W_{gv}):

$$W_{gv} = \frac{dm_{gb}}{dt} = \rho_{gb}\frac{dV_b}{dt} \tag{10}$$

Furthermore, the average gas phase velocity through the vertical vent pipes is given by:

$$\bar{u}_{gv} = \frac{W_{gv}}{A_V\bar{\rho}_g} \tag{11}$$

3.2.3. Bubble rise velocity and bubble breakthrough time

The bubble rise velocity through a stagnant pool of water is obtained by accounting for the forces acting on the bubble due to inertia, buoyancy, and drag (Joseph, 2003; Wallis, 1969). That is:

$$\rho_g V_b\frac{du_b}{dt} = \rho_f g V_b - \rho_g g V_b - \frac{1}{2}C_D\rho_f A_b u_b^2 \tag{12}$$

$$\frac{du_b}{dt} = \frac{(\rho_f - \rho_g)}{\rho_g}g - \frac{1}{2}C_D\frac{\rho_f}{\rho_g}\frac{A_b}{V_b}u_b^2 \tag{13}$$

The drag coefficient (C_D) depends on the relative velocity, size, and shape of the bubble and the fluid properties. The gas bubble formed at the exit of the horizontal vent is assumed to rise at its terminal velocity (i.e., assuming that the bubble's acceleration is negligible) through the suppression pool. Appendix B shows that the bubble accelerates very rapidly and approaches the terminal velocity in a negligibly small duration of time compared to the time required for a bubble breakthrough (i.e., the breakthrough time is several orders of magnitude longer compared to the characteristic time for the bubble to reach its terminal velocity). Consequently, the assumption that the bubble rises at its terminal velocity is justified and appropriate. The terminal velocity of the bubble is obtained from Eq. (13) by setting the inertia term to zero (i.e., $du_b/dt = 0.0$). Therefore:

$$u_{tb} = \sqrt{\frac{2V_b(\rho_f - \rho_g)g}{C_D\rho_f A_b}} = \sqrt{\frac{2V_b g}{C_D A_b}} \tag{14}$$

The gas bubble that is formed at the exit of the horizontal vents appears to rise as a spherical cap bubble due to its relatively large size. Therefore, a cap bubble drag coefficient (8/3) can be used. This is derived based on the theoretical analysis of a spherical cap bubble having an included angle of about 100 degrees and a relatively flat tail (Clift et al., 1978; Wallis, 1969) and is applicable to the bubble Reynolds number greater than 150 (i.e., $Re_b = 2R\rho_f u_b/\mu_f > 150$) of the bubble. Therefore, the terminal velocity of a spherical cap bubble (u_{tbCAP}) of an equivalent spherical radius R is governed by:

$$u_{tb} = u_{tbCAP} = \frac{dz}{dt} = \sqrt{Rg} \tag{15}$$

The above equation can be used directly to obtain the rise velocity of a bubble that is formed at the exit of the horizontal vents. However, the size of the bubble increases (due to the continuous flow of drywell gas and the bubble's expansion) as it rises through the suppression pool. If the bubble grows and reaches the suppression pool structural boundaries, its shape will change from an initial spherical cap to a slug bubble. The transition from the shape of a spherical cap to a slug bubble and the terminal velocity of a slug bubble are governed by the geometry of the suppression pool. Similar to the terminal velocity relationship of the spherical cap bubble [Eq. (15)], empirical correlations are available in the literature for estimating the terminal velocity of the slug bubble (Wallis, 1969). These correlations are dependent on the geometry of the flow channel. Wallis (1969) provides correlations for rectangular and circular geometries. Fig. 4 shows that each 10-degree sector of the ABWR suppression pool (corresponding to one vertical vent and associated top, middle, and bottom horizontal vents) is shaped as an approximately similar trapezoid.

A correlation for the terminal velocity of slug bubbles (u_{tbSLUG}) for a trapezoidal shape is not available in the literature. Therefore,

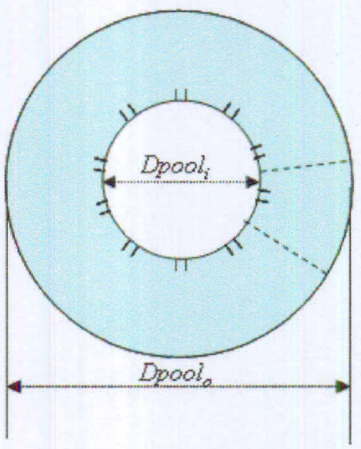

Fig. 4. Cross section of the ABWR suppression pool.

the present model uses the following correlation based on tests in rectangular geometry (Wallis, 1969):

$$u_{tb} = u_{tbSLUG} = k\sqrt{\frac{D_l(\rho_f - \rho_g)g}{\rho_f}} \tag{16a}$$

and

$$k = 0.23 + 0.13\frac{D_s}{D_l} \tag{16b}$$

Before the transition from a spherical cap to a slug bubble, the following equations are used to calculate the lengths of the shorter (D_s) and the longer (D_l) sides of the rectangle in Eq. (16):

$$D_s = \frac{\pi(Dpool_i + Dpool_o)}{2 \times N} \tag{17}$$

$$D_l = \frac{(Dpool_o - Dpool_i)}{2} \tag{18}$$

After the transition from a spherical cap to a slug bubble takes place, the slug bubbles from the neighboring sectors are assumed to coalesce and form a large slug bubble that spans the entire cross section of the suppression pool. Fig. 5 shows that the entire suppression pool cross section can be approximated by a trapezoid. Therefore, the following equations can be used to calculate D_s and D_l in Eq. (16):

$$D_s = \frac{(Dpool_o - Dpool_i)}{2} \tag{19}$$

$$D_l = \frac{\pi(Dpool_i + Dpool_o)}{2} \tag{20}$$

The bubble rise velocity is calculated using the slug bubble terminal velocity correlation [Eq. (16)] as soon as the transition from a spherical cap to a slug bubble is predicted to occur. However, an established criterion for predicting this transition in a rectangular test section is not available. For the present pool swell evaluation model, the transition is assumed to take place as soon as the diameter of the cap bubble exceeds the average of the above estimated lengths of the longer and shorter sides of the rectangle:

$$2R_{cap} \geq \frac{D_s + D_l}{2} \tag{21}$$

The cap bubble radius (R_{cap}) can be estimated from the equivalent spherical bubble radius R. For a spherical cap bubble with an included angle of about 100 degrees and a flat tail, the following relation can be obtained that correlates the radius of the cap bubble with the radius of the spherical bubble (Wallis, 1969):

$$R_{cap} = 2.26 \times R \tag{22}$$

The terminal velocity of the slug bubble is governed by Eq. (16) if the bubble is rising through a stagnant pool of liquid. However, if the channel top is open to the atmosphere (e.g., the PSTF test facility; Yan and Bolger, 2010), the liquid ahead of the rising slug bubble is not expected to remain stagnant (Wallis, 1969). Under this condition, the rise velocity of the slug bubble is augmented by the velocity of the liquid ahead of the expanding and moving bubble. Consequently, the effective slug bubble rise velocity will be equal to the sum of the terminal velocity of the slug bubble and the pool surface velocity:

$$u_{tb} = u_{tbSLUG} + u_{SP} \tag{23}$$

After estimating the bubble rise velocity, the elevation of the bubble is obtained using:

$$Z_{bubble} = \int_0^t \frac{dz}{dt}dt = \int_0^t u_{tb}\ dt \tag{24}$$

where Z_{bubble} is the bubble elevation above the top vent centerline.

The bubble breakthrough time is defined as the time at which the bubble's top surface penetrates the suppression pool surface. At the time of the bubble breakthrough, the thickness of the liquid slug on top of the rising bubble approaches zero. The liquid slug thickness is obtained by subtracting the elevation of the top surface of the bubble from the elevation of the pool surface (see Fig. 3 and Eq. (28)):

$$H_{SL} = (H_s + H_{PS}) - (Z_{bubble} + R) \tag{25}$$

The bubble breakthrough is assumed to occur as soon as H_{SL} reaches zero. The top vent centerline submergence height (H_S) accounts for the rise in pool surface elevation due to the transfer of water from the vent system to the pressure suppression pool. The suppression pool swell height (H_{PS}) is estimated using Eq. (27).

3.2.4. Pressure suppression pool surface velocity and elevation

As noted earlier, the pressure suppression pool surface velocity and elevation are the most important pool swell parameters from a containment and structural design standpoint. The rising pool surface will sweep out a volume that corresponds to the growth in volume of the submerged bubbles. For a total suppression pool surface area of A_{SP}, a total number of N vents feeding N submerged bubbles with a volume growth rate of Eq. (8) will result in a pool surface rise in velocity of:

$$\bar{u}_{SP} = \frac{dH_P}{dt} = \frac{N}{A_{SP}}\dot{V}_b \tag{26}$$

Eq. (26) is integrated to obtain the pressure suppression pool swell height (i.e., the pool surface rise above the initial pool surface elevation):

$$H_{PS} = \int_0^t \frac{dH_P}{dt}dt \tag{27}$$

The elevation of the pressure suppression pool surface above the bottom of the pool is obtained from the following equation:

$$Z_{pool} = H_s + H_{PS} \tag{28}$$

3.2.5. Wetwell gas space pressurization and the outside pressure of the bubble

The pressurization of the wetwell gas space volume due to pressure suppression pool surface rise is calculated by assuming the polytropic compression of an ideal gas:

$$P_{WW} = P^0_{WW}\left(\frac{V^0_{WW}}{V_{WW}}\right)^{\gamma} \tag{29}$$

Wetwell gas space volume is obtained by:

$$V_{WW} = V^0_{WW} - (Z^0_{pool} - Z_{pool}) \times A_{SP} \tag{30}$$

The assumption of an adiabatic compression ($\gamma = 1.4$) will result in a relatively higher wetwell gas space pressure and a lower pool swell height and pool surface velocity. The assumption of isothermal compression ($\gamma = 1.0$) will result in a relatively lower wetwell gas space pressure and a higher pool swell height and pool surface velocity.

The equation to estimate the outside pressure of the bubble, P_∞, is obtained by integrating the averaged area momentum equation [Eq. (1)] over the thickness of the liquid slug that is residing on top of the rising bubble:

$$H_{SL}\rho_f\frac{d\bar{u}_{SP}}{dt} = (P_\infty - P_{WW}) - (H_{SL} + R)\rho_f g - \left(\frac{fH_{SL}}{D_{SP}} + k_{SP}\right)\frac{\bar{u}^2_{SP}}{2}\rho_f \tag{31}$$

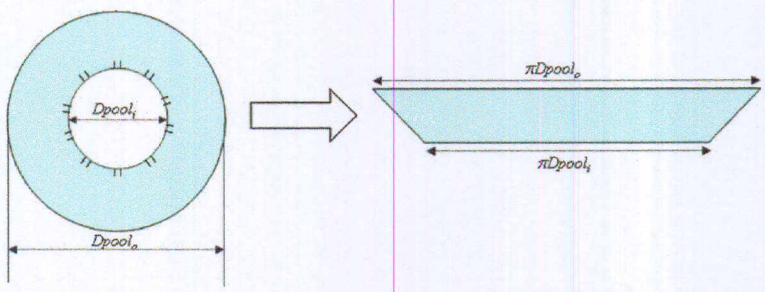

Fig. 5. Cross section of the ABWR suppression pool after transitioning from a spherical cap to a slug bubble shape.

Therefore, the pressure that is exerting on the bubble from the outside is governed by:

$$P_\infty = P_{WW} + H_{SL}\rho_f \frac{d\bar{u}_{SP}}{dt} + (H_{SL}+R)\rho_f g + \left(\frac{fH_{SL}}{D_{SP}} + k_{SP}\right)\frac{\bar{u}_{SP}^2}{2}\rho_f \tag{32}$$

Even though this equation accounts for the frictional losses, these losses are nonetheless negligible. Furthermore, since the area of the pressure suppression pool remains constant, the pressure loss due to spatial acceleration is zero. Note that the gravitational pressure drop is calculated from the center of the expanding bubble.

3.2.6. Closure relations

3.2.6.1. Critical flow. The gas phase can approach the sonic velocity inside the vertical vent pipe. The sonic velocity of the gas phase at the drywell pressure is estimated using (McCabe et al., 1993):

$$u_{gS} = \left(\frac{2}{\gamma+1}\right)^{\gamma+1/2(\gamma-1)} \sqrt{\gamma \frac{P_D}{\rho_{gD}}} \tag{33}$$

The critical mass flow rate for the flow of gas through the vertical vent pipes at the drywell pressure P_D is calculated by:

$$W_{gCR} = A_V \rho_{gD} u_{gS} \tag{34}$$

If the gas flow rate through the vents calculated by Eq. (10) becomes greater than the critical mass flow rate (W_{gCR}), the growth rate of the bubble is limited to the critical mass flow rate and is calculated using the following equation (instead of [Eq. (7)]):

$$\frac{dR}{dt} = \frac{W_{gCR}}{4\pi R^2 \bar{\rho}_g} \tag{35}$$

3.2.6.2. Wall friction factor. The wall friction factor [in Eqs. (6) and (32)] is calculated using the following relations:

$$f = \frac{64}{Re} \quad \text{for } Re \le 2100 \tag{36}$$

$$f = 0.312(Re)^{-0.25} \quad \text{for } 2100 \le Re \le 2\times 10^4 \tag{37}$$

$$f = 0.184(Re)^{-0.2} \quad \text{for } Re \ge 2\times 10^4 \tag{38}$$

3.2.6.3. Equation of state. The drywell gas density is obtained from the pressure and temperature of the drywell:

$$\rho_{gD} = \rho_{gD}(P_D, T_D) \tag{39}$$

The gas density corresponds to the inside pressure of the bubble, which is obtained by assuming a polytropic compression of an ideal gas:

$$\rho_{gB} = \rho_{gB}^0 \left(\frac{P_B}{P_B^0}\right)^{1/\gamma} \tag{40}$$

The average gas density used in the vent pressure drop equation [Eq. (6b)] is obtained from:

$$\bar{\rho}_g = \frac{1}{2}(\rho_{gD} + \rho_{gB}) \tag{41}$$

Furthermore, the pressure suppression pool density is calculated as a function of the water temperature:

$$\rho_f = \rho_f(T_{SP}) \tag{42}$$

4. Application to the ABWR

The proposed model equations are solved numerically to analyze the pressure suppression pool hydrodynamics in the ABWR containment, as discussed in this section. These analyses include best estimate and sensitivity calculations (see Sections 4.2.1 and 4.2.2). The sensitivity calculations are performed to study the impact of key model assumptions on the pool swell parameters. Furthermore, the model predictions are also compared with comparable results based on GOTHIC calculations, as documented in the STP Units 3 and 4 FSAR (2007).

4.1. Initial and boundary conditions

Table 2 lists the initial conditions and key geometrical parameters of the ABWR containment. Initially, the entire containment atmosphere is assumed to be filled with nitrogen, which is also assumed to represent the composition of the gas that flows from the drywell into the suppression pool. During a LOCA, in addition to nitrogen, some steam and suspended water droplets that enter the drywell through the reactor coolant system break can also flow along with the nitrogen into the pressure suppression pool. However, the steam and water droplet content is expected to be very small during the time period of interest (i.e., 2–3 s). Furthermore,

Table 2
ABWR containment initial conditions and key geometric parameters.

Geometric parameters/initial conditions	Value
Initial drywell pressure, kPa	106.0
Initial drywell temperature, K	330.0
Drywell atmosphere composition (nitrogen), %	100
Suppression pool water temperature, K	308.0
Wetwell atmosphere composition (nitrogen), %	100
Initial wetwell gas space temperature, K	308.0
Initial wetwell gas space pressure, kPa	106.5
Top vent centerline submergence, m	3.5
Middle vent centerline submergence, m	4.85
Bottom vent centerline submergence, m	6.2
Initial wetwell gas free volume, m^3	5958.0
Total suppression pool surface area, m^2	507.0
Vent area of one vertical vent, m^2	1.13
Diameter of horizontal vent, m	0.7
Total number vertical vents	10
Total number of horizontal vents	30

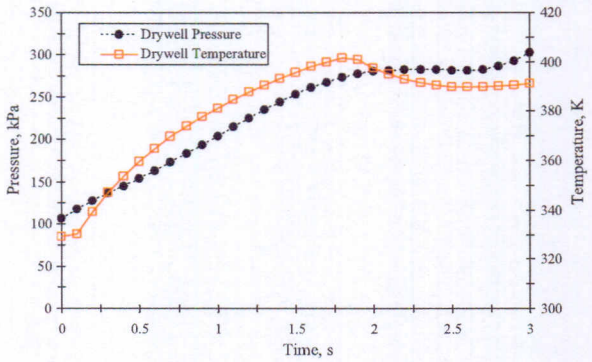

Fig. 6. Drywell pressure and temperature boundary conditions.

the assumption of all nitrogen in the containment atmosphere is expected to result in more bounding estimates of the pool hydrodynamic response behavior.

Due to the short period of the pool swell dynamic, the impact of heat transfer from the suppression pool and wetwell gas space to the wetwell structures is considered to be negligible in the current analysis. As noted earlier in Section 3, the drywell pressure and temperature transients are supplied as boundary conditions to the model. Fig. 6 shows the drywell pressure and temperature boundary conditions used in the current analyses. These boundary conditions are derived from the STP Units 3 and 4 FSAR (2007), which provides pressure and temperature transient data in the drywell and wetwell for the design-basis feedwater and main steam line break accidents. The pressure and temperature curves shown in Fig. 6 are considered to represent the upper bounds of the drywell pressure and temperature conditions.

4.2. Results

4.2.1. Vent clearance time sensitivity calculations

The vent clearance equations presented in Section 3.1 account for the pressure losses due to fluid inertia, spatial acceleration, friction, and hydrostatic head. To assess the sensitivity of the vent clearance time to the contribution from various pressure loss terms, a series of sensitivity calculations was performed using the different forms of the vent clearance equation [Eq. (4)]. Table 3 shows the summary of these calculations. The first column tabulates the form of vent clearance equation that was used, and the second column shows the corresponding vent clearance time predicted for the top vents.

In Table 3, the results show that the vent clearance time is mainly influenced by the pressure losses due to fluid inertia and hydrostatic head. The top vents clear very quickly if only the contribution from the hydrostatic head is considered. These results indicate that the drywell pressure increases to the pressure equivalent to the hydrostatic head of water inside the suppression pool within approximately 0.36 s following a large-break LOCA. Accounting for the inertia of the water column inside the vertical vent pipes and the horizontal vents (the inertia of water inside the suppression pool is negligible due to the relatively large area) results in an increase in vent clearance time from 0.36 to 1.13 s. This increase shows the importance of fluid inertia for an accurate prediction of the vent clearance time. As shown in Table 3, the pressure losses due to friction and spatial acceleration have a negligible contribution to the predicted vent clearance time.

4.2.2. Pool swell sensitivity calculations

Best estimate (base case) and sensitivity calculations were performed for the ABWR containment to assess the impact of various model inputs on the calculations of various pool swell parameters. The model input parameters/assumptions that were selected for the sensitivity calculations include (a) the pressure suppression pool surface area, (b) the polytropic constant for wetwell gas compression, and (c) the effective vent form loss coefficient.

The best estimate values of these parameters were used for the base case calculations. Fig. 1 shows that the horizontal vents in the ABWR containment are located on the inner wall of the annular pressure suppression pool. Due to this configuration of the vents, the air bubbles that formed inside the suppression pool following the discharge of the drywell gas mixture through the horizontal vents do not extend uniformly across the entire pool, which leads to the radially non-uniform swelling of the pool. Consequently, the pool swell has a higher rise near the inside radius of the suppression pool. As a result, the thickness of the liquid slug on top of the bubble is also not uniform across the suppression pool cross section. The GE PICSM code (used for the ABWR DCD pool swell analysis) as stated in ABWR DCD (1997), does not account for the non-uniform pool swell due to its one-dimensional nature. Therefore, GE proposed the assumption of an 80% pool surface area for ABWR DCD (1997) pool swell analysis based on the results of a comparison with/against experiment data. The STP Units 3 and 4 FSAR (2007) GOTHIC pool swell analysis methodology is also based on a one-dimensional nodalization of the suppression pool. Therefore, these analyses also incorporate the 80% pool surface area assumption. For the current model, the best estimate (or base case) simulations that are presented in this section use the 100% value of the pool surface area. However, similar to ABWR DCD (1997) and the STP Units 3 and 4 FSAR (2007) pool swell analyses, in order to account for the effect of the non-uniform pool swell within the present one-dimensional modeling framework, the results of a sensitivity calculation that also assumes an 80% value for the pool surface area are presented.

The polytropic gas constant used in Eq. (29) affects the wetwell gas space compression. As noted earlier, $\gamma = 1.4$ is equivalent to assuming an adiabatic compression (for nitrogen gas) and $\gamma = 1.0$ is equivalent to assuming an isothermal compression. The adiabatic compression assumption ($\gamma = 1.4$) results in a relatively higher wetwell gas space pressure and a lower pool swell and pool surface velocity (due to a higher wetwell gas space pressure). The assumption of isothermal compression ($\gamma = 1.0$) results in a relatively higher suppression pool swell and pool surface velocity and

Table 3
Summary of vent clearance time calculations for the ABWR containment.

Case	Vent clearance equation assumption	Vent clearance time, s
1	Only hydrostatic pressure drop considered $0.0 = (P_D - P_W) + \rho_f g_z (x - H_{S0})$	0.36
2	Hydrostatic + inertial pressure drop considered $\left(\rho_f x + \rho_f L \frac{A_W}{A_H}\right) \frac{d\bar{u}_V}{dt} = (P_D - P_W) + \rho_f g_z (x - H_{S0})$	1.13
3	Hydrostatic + inertial + frictional pressure drop considered $\left(\rho_f x + \rho_f L \frac{A_W}{A_H}\right) \frac{d\bar{u}_V}{dt} = (P_D - P_W) - \rho_f k_{fE} \frac{\bar{u}_V^2}{2} + \rho_f g_z (x - H_{S0})$	1.18
4	Hydrostatic + inertial + spatial acceleration + frictional pressure drop considered $\left(\rho_f x + \rho_f L \frac{A_W}{A_H}\right) \frac{d\bar{u}_V}{dt} - \rho_f \bar{u}_V^2 = (P_D - P_W) - \rho_f k_{fE} \frac{\bar{u}_V^2}{2} + \rho_f g_z (x - H_{S0})$	1.12

Table 4
Results of best estimate and sensitivity case calculations.

Parameters	Base case	Sensitivity cases		
		1	2	3
Pressure suppression pool surface area, %	100	80.0	100	100
Polytropic constant for wetwell gas compression	1.4	1.4	1.0	1.4
Effective vent form loss coefficient				
Top vent open	14.9	14.9	14.9	0.1
Top and middle vents open	5.9	5.9	5.9	0.1
All vents open	4.3	4.3	4.3	0.1
Calculated breakthrough time, s	1.7	1.8	1.7	1.8
Calculated maximum pool swell, m	1.5	2.3	1.5	3.1
Calculated maximum pool surface velocity, m/s	4.3	5.4	4.5	6.8
Calculated maximum bubble pressure, kPa	153	158	148	184
Calculated maximum wetwell gas space pressure, kPa	129	134	122	163

a lower wetwell gas space pressure. The time duration of the pool swell phenomena is about 2–3 s. Consequently, the transfer of heat between the wetwell gas space and the wetwell heat structures are not significant. Therefore, for the best estimate (base case) analysis, the adiabatic compression ($\gamma = 1.4$) is assumed.

The calculated effective form loss coefficients for the gas and liquid flows through the vent system use the modeling approach presented in Appendix A. The vent clearance analysis presented in Section 4.2.1 shows that the vent clearance phenomenon is not sensitive to the frictional and form losses inside the vent system. Therefore, a sensitivity analysis using the liquid flow effective vent form loss coefficient is not required. A sensitivity calculation uses different values for the effective gas phase vent form loss coefficient. The best estimate values of the effective gas flow vent form loss coefficient are calculated using the approach presented in Appendix A. The calculated effective vent form loss coefficient varies from 4.3 to 14.9 depending on the number of horizontal vents that are open. These values are used for the base case calculation. For the sensitivity case calculation, a negligibly small (around 0.1) form loss is assumed under all vent flow configurations.

Table 4 shows the results of the best estimate (base case) and sensitivity case pool swell calculations and the values of the sensitivity parameters used in each calculation. For each calculation, the table also shows the predicted bubble breakthrough time, maximum pool swell height, maximum pool surface velocity, maximum bubble pressure, and maximum wetwell gas space pressure.

The sensitivity case calculation with an 80% pool surface area shows a substantial increase in the maximum pool surface velocity and pool swell height. The maximum pool surface velocity is increased by 25% and the maximum pool swell rise height is increased by 53% compared to the predictions for the base case. Furthermore, the maximum bubble inside pressure and the maximum wetwell gas space pressure remain relatively unaffected (an increase of about 3%) by the reduction in the effective pool surface area. It should be noted that for the sensitivity calculation, even though the suppression pool surface area was reduced by 80%, the wetwell free gas volume was the same as in the base case calculation. In summary, the uneven pool swell (as simulated by the 80% pool surface area sensitivity calculation) results in a higher local pool surface rise and pool surface velocity, but the effects on the pressure of the wetwell gas space and the inside pressure of the bubble are negligible. Since this assumption would result in more bounding value of the estimated pool swell parameters, it is relevant for the design basis pool swell analysis.

The results of sensitivity case calculation with the isothermal compression of the wetwell gas space (i.e., polytropic constant, $\gamma = 1.0$) show a small increase in the maximum pool surface velocity (4.5%). Furthermore, the maximum wetwell gas space and bubble pressures are reduced (−3 to −5%) when compared to the base case results. Therefore, for the design-basis analysis, the assumption of isothermal wetwell gas space compression is more bounding in terms of maximum pool surface velocity, and the assumption of adiabatic wetwell gas space compression (same as the base case) is more bounding in terms of maximum wetwell gas space pressure. However, the overall impact of this assumption is considered to be negligible.

Table 5
Comparison with STP Units 3 and 4 FSAR (2007) results.

Pool swell model parameter	STP units 3 and 4 FSAR (2007)	Present model
Maximum pool swell height, m	8.8	8.7
Maximum pool surface velocity, m/s	10.9	9.5
Maximum wetwell gas pressure, kPaG	146	161
Maximum bubble pressure, kPaG	195	179

The most significant effect on the all pool swell parameters is observed in a sensitivity case with an effective vent form loss coefficient value of 0.1. Table 4 shows that the maximum pool swell is increased/increases by 106% in this sensitivity calculation. Similarly, the maximum pool surface velocity increases by 58%; and the maximum wetwell gas space and bubble pressures increase by more than 20%. The bubble breakthrough time for this sensitivity calculation also increases. The gas flow rate through the vertical vent pipes reaches critical condition due to the very small vent system pressure drop assumed for this calculation. Therefore, the assumption of a smaller effective vent form loss coefficient is more bounding for the prediction pool swell dynamics under DBA conditions.

4.2.3. Comparison to licensing analyses

The STP Units 3 and 4 FSAR (2007) pool swell licensing analysis for the ABWR containment was performed using the GOTHIC code. Table 5 shows the comparison of peak values estimated for the pool swell height, pool surface velocity, wetwell gas space pres-

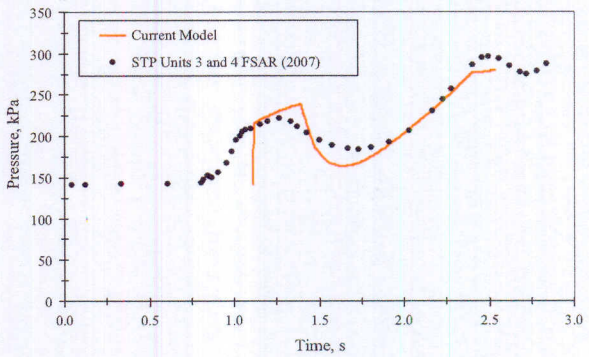

Fig. 7. Comparison with STP Units 3 and 4 FSAR (2007) results: bubble pressure.

Table 6
Comparison with PSTF experiment data.

Calculated model parameter		Percentage of experimental data points predicted by model that are within:	
		<±10%	±10% < and < ±30%
Time of vent clearance	Top vent	100	0
	Middle vent	80	20
	Bottom vent	0	100
Liquid slug thickness	Liquid slug thickness	44	51
Breakthrough elevation	Breakthrough elevation	100	0
Pool surface elevation	Pool surface elevation	100	0
Pool surface velocity	Pool surface velocity	0	100

sure, and bubble pressure in the STP Units 3 and 4 FSAR (2007) GOTHIC analysis and those based on the present model. Generally, good agreement in the results is noted. In Fig. 7, time-dependant bubble pressure predicted by the present model is compared to the STP Units 3 and 4 results. This comparison shows a reasonable agreement.

4.2.4. Comparison to experimental data

The present model is also compared to the BWR Mark III containment PSTF experimental data. Fig. 8 shows a schematic of the one-third scale PSTF test section (Yan and Bolger, 2010). The facility was designed and operated by GE and was used to generate the experimental data in support of the Mark III pressure suppression containment design. The facility consisted of an integrated system of the boiler or pressurizer, drywell, vent system, and wetwell (suppression pool and wetwell gas space). The pool and vent systems both represented one-third scale mockups of an 8-degree sector of the Mark III containment. The transient responses of the pressurizer, drywell, vent system, suppression pool, and wetwell airspace were measured using instruments that included pressure and differential pressure transducers, thermocouples, and conductivity probes. The conductivity probes were used to monitor the liquid interface movement based on the difference in conductance between gas (air and/or steam) and liquid (water). These measurements were further analyzed to obtain data on pool swell parameters (i.e., pool surface elevation, pool surface velocity, and liquid slug thickness).

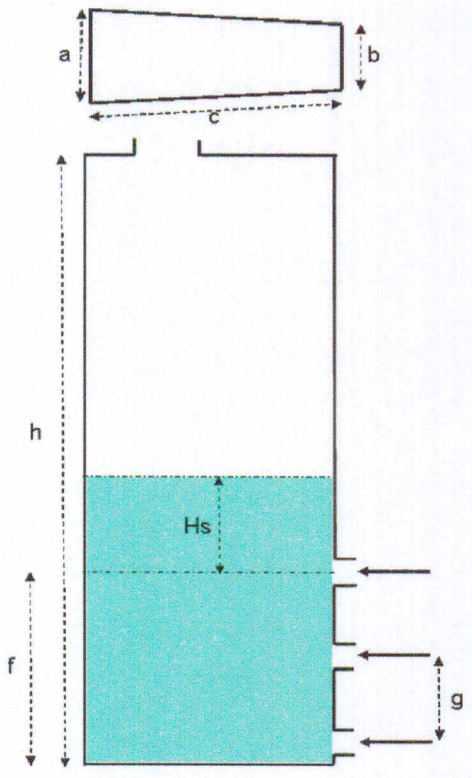

Fig. 8. Schematic of the one-third scale PSTF test facility (Yan and Bolger, 2010).

Three PSTF experiments were selected for the comparison. The selected experiments used air as the blowdown fluid. Table 6 shows summary of the comparison results (detailed comparison could not be presented here due to the proprietary nature of the experimental data). As shown in Table 6, the vent clearance time for the top vent, pool swell height, and the bubble breakthrough elevation are within 10% of the experimental data. The liquid slug thickness and the pool surface velocity are predicted within 30% of the experimental data.

Large deviation in prediction of the pool surface velocity can be due to relatively large uncertainties involved in the measurement of this parameter. The pool surface velocity was not directly measured, instead it was calculated using the measured time for the pool level or interface to travel from one conductance probe to another conductance probe (located downstream) and the distance between the two probes. Therefore, the measurement of pool surface velocity involves uncertainties due to measurements of two conductance probes and a distance between the two probes, which are typically large.

The vent clearance times predicted for the top and middle vents are close to those in the experimental data. However, the model predicted a very early clearance of the bottom horizontal vent compared to the experimental data. For the model, the vent clearance is assumed to occur as soon as the water level inside the vertical vent pipe drops below the top elevations of the horizontal vents (shown by the dotted lines in the figure). The discrepancy between the prediction and measurement of the vent clearance times can be due to several simplifying vent clearance model assumptions (see Section 3.1). These assumptions start to breakdown following the opening of the top horizontal vent. Immediately after the clearance of the top vent, the drywell air begins to flow into the suppression pool and creates an expanding air bubble at the exit of the vent. This expanding bubble accelerates the pool surface and exerts a higher pressure on the middle and bottom vent exits, which delays their clearance. Therefore, the assumptions of a negligible pool surface velocity and an inertial pressure drop inside the suppression pool may not be fully applicable following the clearance of the top horizontal vent. Consequently, the model predicts an early clearance of the middle and bottom horizontal vents. Furthermore, as noted earlier, the model assumes the clearance of the horizontal vent as soon as the water level inside the vertical vent drops below the top elevation of the horizontal vent. However, the experimental data show that after the water level drops below the top elevation of the horizontal vent, the air–water interface enters into the horizontal vent and moves toward the exit with the increasing drywell pressure. Therefore, the air–water interface requires a finite time to travel from the entrance to the exit of the horizontal vent. The movement

of the interface through the vent is not included in the model. This effect is more pronounced in the PSTF experiments because of the larger length-to-diameter ratio of the horizontal vents in the PSTF experiments as compared to the ABWR containment design.

In summary, the model prediction of the clearance for the top and the middle horizontal vents is reasonable. The earlier prediction of the clearance for the bottom horizontal vent is due to modeling assumptions and limitations. Furthermore, this model characteristic of the pool swell analysis is bounding because the earlier clearance of the bottom horizontal vents would result in the transfer of a larger amount of drywell atmosphere into the suppression pool, thus resulting in larger hydrodynamic loads.

5. Conclusion

A PIRT applicable to the ABWR containment pool swell analysis was used as a basis for the development of an analytic model to predict important pool swell parameters. The highly ranked phenomena were represented mechanistically. The present model enables the calculation of the vent clearance time and various pressure suppression pool swell parameters including the pressure suppression pool surface velocity, the surface elevation, the gas bubble pressure, and the wetwell gas space pressure. The model was applied to conditions of a large-break LOCA in the ABWR containment. Sensitivity calculations were performed to assess the impact of key model assumptions on various pool swell parameters. The vent clearance time sensitivity analysis showed that the vent clearance phenomenon is significantly influenced by the hydrostatic head and the inertia of water residing inside the vent system. Furthermore, the pool swell analysis sensitivity calculations show that the assumption of a smaller pool surface area (to account for the uneven pool swell) and reduced vent loss coefficients are the most bounding in terms of their impact on the calculation of suppression pool swell parameters. Finally, the model was applied to conditions corresponding to a LOCA inside the ABWR containment. Comparisons of the calculated results to those of other studies and to the PSTF experimental data showed reasonable agreement. The model predicted vent clearance time for the top vents, the pool swell height, and the bubble breakthrough elevation are within 10% of the experimental data. The predicted pool surface velocity and the liquid slug thickness are within 30% of the experimental measurements.

Acknowledgements

The authors acknowledge the significant contributions of Dr. Fredrick Moody (Consultant and formerly with General Electric Company) in preparing the PIRT used herein, and the valuable inputs provided by Mr. Andrzej Drozd of the United States Nuclear Regulatory Commission, Office of New Reactors.

This work was performed under the auspices of the United States Nuclear Regulatory Commission, Office of New Reactors (Contract Number NRC-42-07-483).

Appendix A. Effective vent form loss coefficient

The effective vent form loss coefficients for the flow of gas and liquid phases through the vent system are estimated by accounting for the geometry of the vent system and the water level inside the vertical vent pipes. This section describes the methodology used to estimate the gas phase effective vent form loss coefficient (k_{gE}). A similar approach is used to estimate the liquid phase effective vent form loss coefficient (k_{fE}).

Fig. A1 illustrates the scenario in which only the top horizontal vents are partially open. The effective vent form loss coefficient for the gas flow (k_{gE}) under this configuration is derived by summing up the drywell connecting vent entrance loss (k_d), the vertical vent pipes to the horizontal vent turning loss (k_t), and the horizontal vent exit loss (k_e). As shown below, the effects of the flow area change for the horizontal vents (due to a decreasing water level inside the vertical vent pipe as the drywell pressure increases, and due to differences in diameters) on the turning loss (k_t) and the exit loss for the horizontal vents (k_e) are also accounted for in the derivation (Crane, 1980):

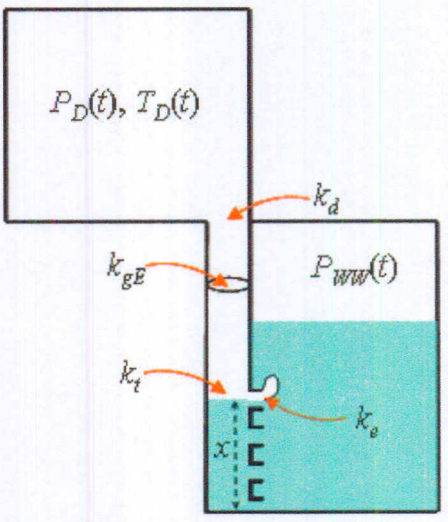

Fig. A1. Estimate of the effective vent form loss coefficient: top vent open.

$$\frac{k_{gE}}{A_V^2} = \frac{k_d}{A_V^2} + \frac{k_t + ((1-\beta_1^2)/2\beta_1^4)}{A_V^2} + \frac{k_e}{A_{Hg1}^2} \tag{A1}$$

Fig. A2 illustrate the scenario in which the top two horizontal vents are open (the middle vents are partially open). With the multiple vents open, the losses through the horizontal vents are

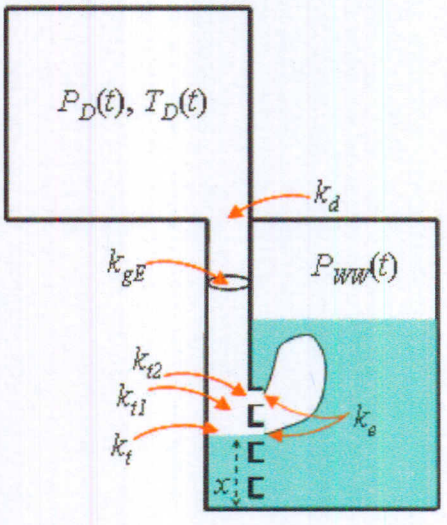

Fig. A2. Estimate of the effective vent form loss coefficient: top two vents are open.

assumed to be parallel. The loss coefficient for the top horizontal vents is defined by:

$$\frac{k_A}{A_V^2} = \frac{k_{t1} + ((1-\beta_1^2)/2\beta_1^4)}{A_V^2} + \frac{k_e}{A_{Hg1}^2} \quad \text{(A2)}$$

As shown in Eq. (A2), the effects of the flow area change for the horizontal vents (due to a difference in the diameter of the horizontal and vertical vent pipes) on the turning loss (k_{t1}) is accounted for in the derivation (Crane, 1980).

The loss coefficient for the middle horizontal vents is defined by:

$$\frac{k_B}{A_V^2} = \frac{k_{t2}}{A_V^2} + \frac{k_t + ((1-\beta_2^2)/2\beta_2^4)}{A_V^2} + \frac{k_e}{A_{Hg2}^2} \quad \text{(A3)}$$

The effective horizontal vent form loss coefficient (k_C) is obtained by:

$$\frac{A_V}{\sqrt{k_C}} = \frac{A_V}{\sqrt{k_A}} + \frac{A_V}{\sqrt{k_B}} \quad \text{(A4)}$$

The total effective vent form loss coefficient for the gas flow (k_{gE}) when the top two vents are open is obtained by summing the drywell connecting vent entrance loss (k_d) and the effective horizontal vent loss (k_C):

$$k_{gE} = k_C + k_d \quad \text{(A5)}$$

A similar approach is used to derive the effective vent form loss coefficient for the gas flow (k_{gE}) when all three vents are open.

Appendix B. Bubble rise velocity

As presented in Section 3.2.3, for the present model, the gas bubble formed at the exit of the horizontal vents is assumed to rise at its terminal velocity (i.e., bubble acceleration zero) through the suppression pool. This Appendix presents the analysis to support the above modeling assumption.

The solution to Eq. (12) is:

$$u_b = a\left(\frac{e^{2abt}-1}{e^{2abt}+1}\right) \quad \text{(B1)}$$

where:

$$a = \sqrt{\frac{2(\rho_f - \rho_g)V_b}{C_D \rho_f A_b}} \quad \text{(B2)}$$

and

$$b = \frac{1}{2} C_D \frac{A_b}{V_b} \frac{\rho_f}{\rho_g} \quad \text{(B3)}$$

The drag coefficient (C_D) depends on the relative velocity, size, and shape of the bubble and the fluid properties.

As noted in Section 3.2.3, the gas bubble that forms at the exit of the horizontal vents appears to rise as a spherical cap bubble due to its relatively large size. Therefore, for the current calculations, the cap bubble drag coefficient (8/3) is used. It is derived based on the theoretical analysis that a spherical cap bubble has an included angle of about 100 degrees and a relatively flat tail (Clift et al., 1978; Wallis, 1969) and is applicable to the bubble Reynolds number greater than 150 (i.e., $Re_b = 2R\rho_f u_b/\mu_f > 150$). Fig. B1 shows the rise velocity of a spherical cap bubble calculated using Eq. (B1). The figure shows that the time required for a bubble to reach the terminal velocity increases with an increase in the size of the bubble. The bubble accelerates very rapidly and approaches the terminal velocity. The maximum calculated characteristic time required for the bubble to reach terminal velocity is less than 2 ms. This characteristic time is negligibly small compared to the time required for a bubble breakthrough (i.e., the breakthrough time is several orders of magnitude longer compared to the characteristic time for the bubble to reach its terminal velocity). Consequently, the assumption that the bubble rises at its terminal velocity is justified and appropriate.

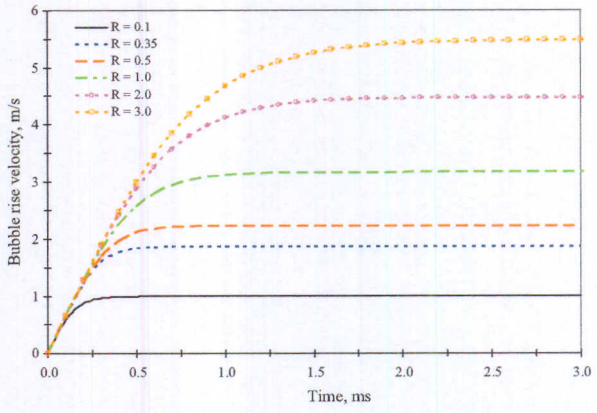

Fig. B1. Rise velocity of the bubble through a stagnant pool of water.

References

ABWR DCD, 1997. ABWR Design Control Document Revision 4. http://www.nrc.gov/reactors/new reactors/design-cert/abwr.html.

Carey, V.P., 2007. Liquid–Vapor Phase–Change Phenomena, second ed. Hemisphere Publishing Corporation, New York.

Chambre, P.L., Nitao, J., 1981. Modeling of the Mark I pool suppression system. Nuclear Engineering and Design 64, 361–379.

Chan, R.K.C., Vander Vorst, M.J., 1978. SWELL3/SURGE: computer models for hydrodynamic response of Mark I suppression pools, final report. EPRI-NP-835.

Chen, C., Dhir, V., 1982. Hydrodynamics of a bubble formed at vent pipe exit. International Journal of Multiphase Flow 8, 147–163.

Clift, R., Grace, J.R., Weber, M.E., 1978. Bubbles, Drops, and Particles. Academic Press, New York.

Crane Co, 1980. Flow of Fluids through Valves, Fittings, and Pipe, second ed. Crane Co Engineering Division, Chicago.

Fernandez, T., 1976. Pool swell in a nuclear containment wetwell. EPRI Journal 1, 21–23.

Final Safety Evaluation Report Related to the Certification of the Advanced Boiling Water Reactor Design, Main Report, 1994. NUREG-1503. http://adamswebsearch2.nrc.gov/idmws/ViewDocByAccession.asp?AccessionNumber=ML080670592.

Glenn, L.A., McMaster, W.H., 1978. BWR pool dynamics in a loss of coolant accident. Calculation of the air-venting phase. UCRL-52435.

Gupta, S., Balewski, B., Fischer, K., Poss, G., 2011. Experimental investigations of BWR suppression pool behaviour under loss of coolant accident conditions. In: Proceedings of International Congress on Advances in Nuclear Power Plants (ICAPP-2011), paper-11389.

Huber, P.W., Sonin, A.A., Anderson, W.G., Burke, R.P., Ruggieri, N.G., 1979. Considerations in small-scale modeling of pool swell in BWR containments. NUREG/CR-1143.

Joseph, D.D., 2003. Rise velocity of a spherical cap bubble. Journal of Fluid Mechanics 488, 213–223.

Kiang, R.L., Grossi, B.J., 1981. Three-dimensional pool-swell modeling of a Mark I suppression system, final report. EPRI-NP-2061.

Kiang, R.L., Jeuck, P.R. III, 1981. Additional pool-swell experiments on a 1/11.7-scale Mark I pressure-suppression model, final report. EPRI-NP-2058.

Kiang, R.L., Jeuck, P.R. III, 1980. Study of pool-swell dynamics in a Mark II single-cell model, final report. EPRI-NP-1353.

Kukita, Y., Namatame, K., Shiba, M., 1984. The LOCA air-injection loads in BWR Mark II pressure suppression containment systems. Nuclear Engineering and Design 77, 117–129.

Lahey Jr., R.T., Moody, F.J., 1993. The Thermal-Hydraulics of a Boiling Water Reactor, second ed. American Nuclear Society, La Grange Park, IL.

Lai, W., McCauley, E.W., 1978. Air scaling and modeling studies for the 1/5 scale Mark I boiling water reactor pressure suppression experiment. Lawrence Livermore Laboratory Report, UCRL-52383.

McCabe, W.L., Smith, J.C., Harriott, P., 1993. Unit Operations in Chemical Engineering, fifth ed. McGraw-Hill, New York.

South Texas Project (STP) Units 3 and 4 FSAR, 2007. South Texas Project Units 3 and 4 COLA (FSAR) Revision 3. http://www.nrc.gov/reactors/new-reactors/col/south-texas-project.html.

Wallis, G.B., 1969. One-Dimensional Two-Phase Flow. McGraw-Hill, New York.

Widener, S.K., 1986. Analytical simulation of boiling water reactor pressure suppression pool swell. Nuclear Technology, 72.

Yan, J., Bolger, F., 2010. Evaluation of pool swell velocity during large break loss of coolant accident in boiling water reactor Mark III containment design. Nuclear Engineering Design 240, 1789–1794.